

An Effective Membrane Model of the Immunological Synapse

Subhadip Raychaudhuri⁽¹⁾, Arup K. Chakraborty^(1,2,3), and Mehran Kardar⁽⁴⁾

⁽¹⁾*Department of Chemical Engineering,*

⁽²⁾*Department of Chemistry,*

⁽³⁾*Material Sciences and Physical Biosciences Divisions,*

Lawrence Berkeley National Laboratory,

University of California Berkeley, Berkeley CA 94720

⁽⁴⁾*Department of Physics,*

Massachusetts Institute of Technology,

Cambridge, MA 02139

(Dated: October 26, 2018)

The immunological synapse is a patterned collection of different types of receptors and ligands that forms in the intercellular junction between T Cells and antigen presenting cells (APCs) during recognition. The synapse is implicated in information transfer between cells, and is characterized by different spatial patterns of receptors at different stages in the life cycle of T cells. We obtain a minimalist model that captures this experimentally observed phenomenology. A functional RG analysis provides further insights.

PACS numbers: 87.16.Dg,64.60.-i

T lymphocytes (T cells) are the orchestrators of the adaptive immune response in complex organisms. A key event during activation of the immune response is T cell recognition of cells that display peptides derived from foreign antigens on their surface [1]. Recent experiments [2, 3, 4, 5, 6] have vividly demonstrated that during this recognition process a highly organized pattern of different types of receptors and ligands forms in the intercellular junction between T cells and antigen presenting cells. This recognition motif is several microns in diameter, and since it is implicated in information transfer between the cells, it is called the immunological synapse. Formation of a synapse is also characteristic of an earlier stage in the life cycle of T cells. Immature T cells (thymocytes) are selected in the thymus so that they are not activated by peptides derived from the organism itself [1]. In the thymus, thymocytes interact with cells that display self peptides on their surface. Thymocytes that bind strongly are deleted by apoptosis. The synapses formed during thymocyte selection are distinctly different in character [7, 8] from those observed during mature T cell activation. Understanding the mechanisms via which synapses form under different circumstances and the biological purpose of creating different spatial patterns of cell surface receptors are active areas of research. In addition to the biological significance, an understanding of these issues may also inspire the creation of synthetic mimics that could carry out biomimetic recognition tasks which could be useful in applications such as targeted drug delivery.

In this letter, starting from a model proposed by Qi et al. [9], we develop a minimalist model that captures some of the essential physics of synapse formation when apposing membranes contain complementary pairs of receptors and ligands. The model allows us to calculate a *phase diagram* which delineates the conditions that lead to a *transition* from synaptic patterns characteristic of mature T cells to those observed during thymocyte selection. This phase diagram may serve as a guide for the design of synthetic analogs.

Consider two membranes containing complementary pairs of receptors and ligands. The intramembrane motion of receptors and ligands is determined either by diffusion or a directed velocity toward the center of the junction [10]. Complementary receptors and ligands can bind to each other if apposed. Different receptor-ligand complexes have different topographical size [11], and hence the rate of association depends upon local intermembrane separation. The receptor-ligand complexes also dissociate at a prescribed rate. For the case where there are only two types of receptors-ligand pairs (TCR-MHCp and LFA1-ICAM1 in the case of the T cell immunological synapse), the pertinent equations are:

$$\begin{aligned}\frac{\partial C_T}{\partial t} &= D_T \nabla^2 C_T - k_{on}(z) C_T C_M + k_{off} C_{TM} - \vec{\nabla} \cdot (\vec{V} C_T), \\ \frac{\partial C_M}{\partial t} &= D_M \nabla^2 C_M - k_{on}(z) C_T C_M + k_{off} C_{TM}, \\ \frac{\partial C_{TM}}{\partial t} &= D_{TM} \nabla \cdot \left[\nabla C_{TM} + \frac{1}{k_B T} C_{TM} \nabla \frac{\delta F}{\delta C_{TM}} \right] + k_{on}(z) C_T C_M - k_{off} C_{TM}, \\ \frac{\partial C_L}{\partial t} &= D_L \nabla^2 C_L - k'_{on}(z) C_L C_I + k'_{off} C_{LI},\end{aligned}$$

$$\begin{aligned}\frac{\partial C_I}{\partial t} &= D_I \nabla^2 C_I - k'_{on}(z) C_L C_I + k'_{off} C_{LI}, \\ \frac{\partial C_{LI}}{\partial t} &= D_{LI} \nabla \cdot \left[\nabla C_{LI} + \frac{1}{k_B T} C_{LI} \nabla \frac{\delta F}{\delta C_{LI}} \right] + k'_{on}(z) C_L C_I - k'_{off} C_{LI}.\end{aligned}\tag{1}$$

Here, C represents the concentration of a given molecule, and z is the separation of the T cell membrane from the APC membrane. The abbreviations used for different protein molecules are: TCR \rightarrow T, MHC_p \rightarrow M, TCR-MHC_p \rightarrow TM, LFA1 \rightarrow L, ICAM1 \rightarrow I, and LFA1-ICAM1 \rightarrow LI. The different species diffuse with the corresponding diffusion coefficients D . \vec{V} is a directed velocity of TCR due to cytoskeletal motion [10]. Since small values of \vec{V} do not change the qualitative physics [12], for simplicity we do not consider this further in this letter. The binding and dissociation chemical reactions are controlled by the rate constants $k_{on}(z)$ and k_{off} . The local intermembrane separation, z , evolves according to a time-dependent Ginzburg-Landau equation,

$$M^{-1} \frac{\partial z}{\partial t} = -\frac{\delta F}{\delta z} + \zeta,\tag{2}$$

where M is a phenomenological parameter for the rate at which membrane shapes respond to changes in the free energy, $F = \int d^2x \left[\frac{\gamma}{2} (\nabla z)^2 + \frac{\kappa}{2} (\nabla^2 z)^2 + C_{TM} B_{TM}(z) + C_{LI} B_{LI}(z) \right]$. The first two terms are due to costs associated with deforming the membranes: If one of the membranes is supported and undeformed, γ and κ are the surface tension and bending rigidity of the free membrane; for similar membranes they are half the corresponding parameters for each membrane. $B_{TM}(z)$ and $B_{LI}(z)$ denote respectively the bond energy gained from forming TM and LI complexes for a specific intermembrane separation z .

The time scales associated with large-scale membrane shape changes can be much slower than those associated with binding kinetics and protein mobility. In such cases, for a given membrane shape, the local species concentrations are related by

$$\begin{aligned}\frac{C_{TM}(z)}{C_T C_M} &= \frac{k_{on}(z)}{k_{off}} = \frac{K_{on}}{K_{off}} \exp \left[-\frac{B_{TM}(z)}{k_B T} \right], \\ \frac{C_{LI}(z)}{C_L C_I} &= \frac{k'_{on}(z)}{k'_{off}} = \frac{K'_{on}}{K'_{off}} \exp \left[-\frac{B_{LI}(z)}{k_B T} \right].\end{aligned}\tag{3}$$

Substituting Eq. (3) in Eq. (2) obtains the following effective dynamical equation for z

$$\begin{aligned}M^{-1} \frac{\partial z}{\partial t} &= \gamma \nabla^2 z - \kappa \nabla^4 z \\ &\quad - \frac{K_{on}}{K_{off}} C_T C_M \exp \left(-\frac{B_{TM}(z)}{k_B T} \right) B'_{TM}(z) \\ &\quad - \frac{K'_{on}}{K'_{off}} C_L C_I \exp \left(-\frac{B_{LI}(z)}{k_B T} \right) B'_{LI}(z) + \zeta.\end{aligned}\tag{4}$$

This corresponds to model A dynamics (Eq. (2)) for the order parameter z with an effective free energy functional

$$\tilde{F} = \int d^2x \left[\frac{\gamma}{2} (\nabla z)^2 + \frac{\kappa}{2} (\nabla^2 z)^2 - k_B T \frac{K_{on}}{K_{off}} C_T C_M e^{-\frac{B_{TM}(z)}{k_B T}} - k_B T \frac{K'_{on}}{K'_{off}} C_L C_I e^{-\frac{B_{LI}(z)}{k_B T}} \right].\tag{5}$$

The reduction of the full set of equations to one determining the separation z is reminiscent of the elimination of counter-ions in constructing the Poisson-Boltzmann equation, where the concentration of counter-ions is obtained from the Boltzmann weight of a potential, itself determined self-consistently from the counterion charge profile. Here z plays the role of the potential, while the protein complexes are analogous to the counterions.

Bound receptor-ligand complexes do not favor membrane shape changes that deform the bond from its natural length. We thus use a harmonic approximation for the functional form of the bond elasticity energy, i.e. $B_i(z) = B_i^0 + \lambda_i (z - z_i)^2/2$, with $i = 1, 2$ for the two possible complexes[9]. The maximal bond energies B_i^0 can be absorbed into K_{on}/K_{off} , and shall be ignored henceforth. The natural lengths of receptor-ligand proteins are taken to be those appropriate for the T cells ($z_1 = z_{TM} = 15nm$ and $z_2 = z_{LI} = 42nm$) [11, 13], with corresponding ‘spring constants’ of λ_i given below. With this approximation, the dynamical Eq. (4) takes the form (measuring time in units such that $M = 1$)

$$\frac{\partial z}{\partial t} = -\frac{\delta}{\delta z} \left\{ \int d^2x \left[\frac{\gamma}{2} (\nabla z)^2 + \frac{\kappa}{2} (\nabla^2 z)^2 + V(z) \right] \right\} + \zeta,\tag{6}$$

with an effective potential

$$V(z) = k_B T \begin{cases} -C_1^* \exp\left\{-\frac{(z-z_1)^2}{2\sigma_1^2}\right\} - C_2^* \exp\left\{-\frac{(z-z_2)^2}{2\sigma_2^2}\right\}, & \text{for } z > 0 \\ c, & \text{for } z < 0. \end{cases} \quad (7)$$

In writing Eq. (7) we have assumed that $\sigma^2 = k_B T / \lambda$, which is appropriate if the curvature of the receptor-ligand interaction potential is the same in the bound state and at the activation barrier. Other assumptions do not alter the qualitative physics. The parameters $C_1^* = (K_{on}/K_{off})C_T C_M$ and $C_2^* = (K'_{on}/K'_{off})C_L C_I$ represent the number of complexes (TM and LI, respectively) formed if the intermembrane separation equals the corresponding optimal bond separation. As depicted in Fig. 1, the effective potential has two minima corresponding to the two possible bonds. Negative separations are prevented by a large energy cost $k_B T c \gg 1$ (hard wall in simulations).

Eq. (6) was solved numerically by a finite difference method. Initially, the upper membrane was assigned a parabolic shape in the contact region, and the intermembrane distance was kept constant ($\sim 50nm$) outside the contact region. For the membrane parameters we use experimentally determined values [14] of $\gamma = 700k_B T / \mu m^2$ and $\kappa = 400k_B T$, and for the bond elasticity we take $\sigma_1 = 13nm$ and $\sigma_2 = 5nm$ [9]. Simulations were carried out for various ratios of C_1^*/C_2^* , and local concentrations of the TCR-MHCp and LFA1-ICAM1 were obtained from the intermembrane separation using Eqs. (3).

Zero Noise: In the absence of noise ($\zeta = 0$), Eq. (6) is a relaxational dynamics toward the minimum of the potential $V(z)$, subject to the imposed boundary conditions. For $C_1^* > C_2^*$ the minimum at z_{TM} is deeper, and indeed in the numerical simulations a central cluster of TCR-MHCp complex forms quickly in the intercellular contact area. As the boundary of the contact region is kept at a constant height close to z_{LI} , the longer LFA1-ICAM1 moves toward the boundary giving rise to a structure very similar to the final synaptic pattern obtained in the experimental and numerical studies [3, 9, 15, 16].

When the concentration C_1^* is below C_2^* , the global minimum of $V(z)$ switches to z_{LI} . In this regime, the receptor-ligand complex LFA1-ICAM1 concentration dominates the entire intercellular junction, and no synaptic pattern is formed. In the noise-less (mean-field) limit the location of the transition between the two patterns is always at $C_1^*/C_2^* = 1$. The patterns obtained and the conditions for transitions between them are quite different when ζ is finite.

Finite Noise: In this case, numerical simulations of Eq. (6) are performed with a random ζ with zero mean, and variance equal to $k_B T$ to mimic thermal noise. Starting with sufficiently large values of $C_1^* \geq C_2^*$, we again find that TCR-MHCp aggregates at the center of the intercellular junction at long times. In Fig. (2a) a cross section of the upper membrane and the associated protein concentrations are shown. Very similar synaptic patterns have been observed [2, 3, 4, 5, 6] for *in vivo* and *in vitro* experiments with mature T cells.

For double positive (DP) thymocytes, the TCR concentration is much lower compared to mature T-cells [7]. This experimental fact corresponds to lower values of C_1^* . When we numerically solve Eq. (6) with $C_1^*/C_2^* < f_c$, the mature

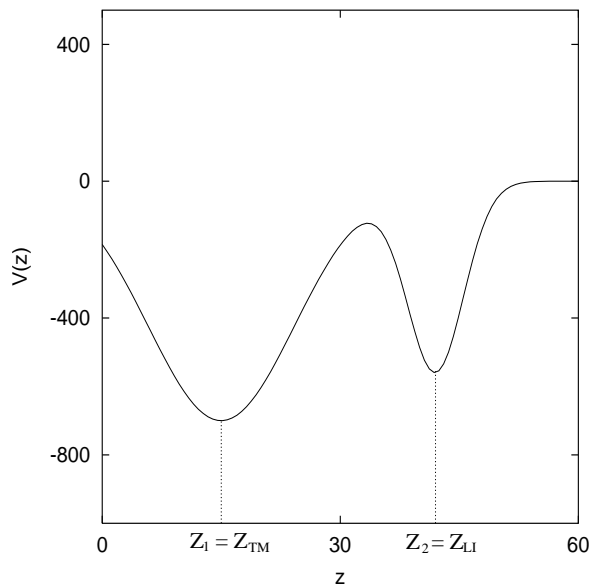


FIG. 1: The effective potential $V(z)$ in Eq. (7).

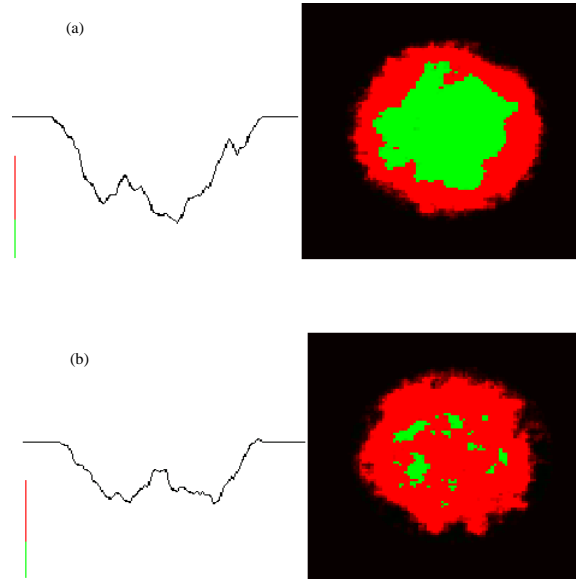


FIG. 2: Right panel: (a) Structure of a mature synapse: TCR-MHCp occupies the central region (represented in green), surrounded by a ring of LFA1-ICAM1 (shown in red). (b) Dynamic accumulation of TCR-MHCp (green) at random places in a sea of LFA1-ICAM1 (red) molecules as observed for thymocytes. Left panel: Height fluctuations corresponding to (a) and (b). The green ($z_{TM} = 15nm$) and red ($z_{LI} = 42nm$) lines are meant to guide the eye.

synapse is never formed. Rather, we observe (see Fig. 2b) fluctuating patterns with fleeting clusters of TCR-MHCp forming at various locations in a sea of LFA1-ICAM1. Note that this pattern is different in character from the one observed for $C_1^*/C_2^* < 1$ in the noiseless case. Such dynamic patterns have been observed in recent experiments using DP thymocytes [7, 8], and can be understood using the simple picture of relaxational motion in a potential with two minima. As we lower the TCR concentration, the minimum at $z = z_{TM}$ becomes shallower, and eventually the minimum near $z = z_{LI}$ corresponds to the global equilibrium. However, thermal fluctuations allow sampling of the region near the minimum at $z = z_{TM}$. This will favor sporadic aggregation of TCR-MHCp at random places. As long as the barrier between the two minima is not very large, such transient fluctuations will be frequent.

The effects of thermal fluctuations can be estimated by expanding $V(z)$ to quadratic order around each of its minima. The total energy cost of a deformation of wavenumber p is given by $E_i(p) = (k_B T C_i^* \sigma_i^{-2} + \gamma p^2 + \kappa p^4) |z(p)|^2$. Integrating out these (Gaussian) fluctuations yields a free energy per unit area of

$$\frac{F_i^*}{k_B T} = C_i^* - \frac{1}{2} \int \frac{dp}{2\pi} p \ln \left(\frac{k_B T C_i^* \sigma_i^{-2} + \gamma p^2 + \kappa p^4}{2\pi k_B T} \right). \quad (8)$$

The location of the transition between the two classes of patterns can now be estimated from $F_1^* = F_2^*$. Thermal noise enhances the minimum with larger σ (width), because of its larger entropy. Hence the more flexible bond is formed more easily when thermal noise is present [17]. Fig. 3 shows that the larger the temperature, the smaller the value of f_c . This “phase diagram” could serve as a guide for the design of synthetic systems as it shows how to manipulate conditions such that synaptic patterns characteristic of mature T cells or thymocytes are realized.

Self consistency of the above quadratic expansion requires that the extent of the fluctuations should be less than the corresponding variance of the bond. The mean square width of the interface trapped around $z = z_i$ is given by

$$W_i^2 = \int \frac{dp}{2\pi} p \frac{k_B T}{k_B T C_i^* \sigma_i^{-2} + \gamma p^2 + \kappa p^4}. \quad (9)$$

Typical values of C_1^* range from $O(10)(\mu m)^{-2}$ for thymocytes to $O(100)(\mu m)^{-2}$ in mature T cells. For this range of parameters, the constant term in the denominator of Eq. (9) dominates, until it is cut-off by the bending rigidity at distances of the order of $1\mu m$. (The overall size of the synapse is of the order of $10\mu m$ [3].) It is then easy to estimate the value of the integral, and we find that the ratios W_1/σ_1 and W_2/σ_2 are of the order of 0.1. While these estimated fluctuations are smaller than the width of the attractive potentials, they are significant enough to make nonlinear corrections to the above quadratic expansion important. Thus the phase diagram in Fig. 3, using Eq. (8) should be regarded as an approximation.

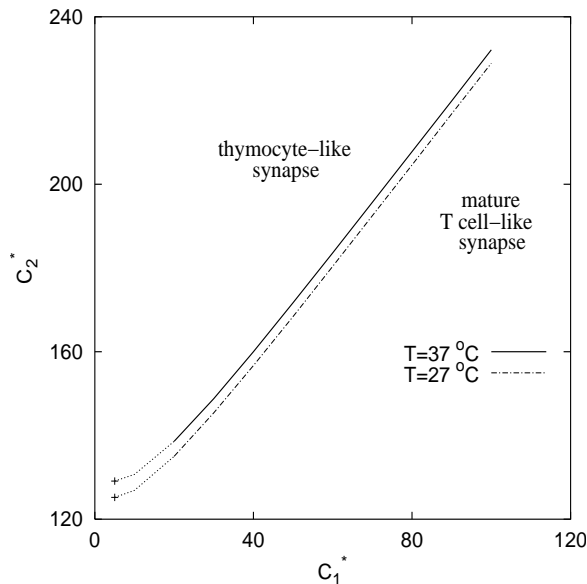


FIG. 3: Phase diagram (projection on the C_1^* - C_2^* plane) for physiological temperature $T = 37^\circ\text{C}$ and room temperature $T = 27^\circ\text{C}$. C_1^* and C_2^* are measured in units of $(\mu\text{m})^{-2}$. The dotted portion of the curves (for low values of C_1^* - C_2^*) is conjectured as explained in the text.

When anharmonic corrections are significant, an alternative approach is to employ a functional renormalization group (RG) scheme used [18, 19, 20] in the context of wetting transitions. It consists of the following steps: (1) The fluctuating field $z(x)$ is divided into two parts corresponding to small wavenumbers ($0 < |p| < \Lambda/b$) and large wavenumbers ($\Lambda/b < |p| < \Lambda$); (2) The large wavenumber fluctuations $\Lambda/b < |p| < \Lambda$ are integrated out to yield a coarse grained Hamiltonian; and (3) The system is rescaled to new coordinates $x' = x/b$ and $z'(x') = z(x)$. (The field z does not need to be scaled in two dimensions.) The second step can only be done approximately, and a first order expansion of the potential $V(z)$ leads to the linear approximation[18]

$$V_b(z) \approx \mathcal{L}[V(z)] = b^2 \int_{-\infty}^{\infty} \frac{dz'}{\sqrt{2\pi}\delta(b)} \exp\left[-\frac{(z-z')^2}{2\delta^2(b)}\right] V(z'). \quad (10)$$

The width of the convolution, $\delta(b)$, is

$$\delta^2(b) = \int_{\Lambda/b}^{\Lambda} \frac{dp}{2\pi} \frac{p}{\gamma p^2 + \kappa p^4} = \frac{k_B T}{4\pi\gamma} \left[2 \ln b - \ln\left(\frac{1 + \kappa\Lambda^2/\gamma}{1 + \kappa\Lambda^2/(b^2\gamma)}\right) \right]. \quad (11)$$

Note that κ is an irrelevant operator in the RG sense (vanishing as b^{-2} under scaling). Indeed the second term in the above equation can be ignored asymptotically for $b \gg 1$, but may be important for quantitative comparisons when the bending rigidity is large.

Applying Eq. (10) to the potential in Eq. (7) yields the renormalized potential

$$V_b(z) \approx b^2 k_B T \left[-\frac{\sigma_1 C_1^*}{\sqrt{\sigma_1^2 + \delta^2}} e^{-\frac{(z-z_1)^2}{2(\sigma_1^2 + \delta^2)}} - \frac{\sigma_2 C_2^*}{\sqrt{\sigma_2^2 + \delta^2}} e^{-\frac{(z-z_2)^2}{2(\sigma_2^2 + \delta^2)}} + c \operatorname{erf}(z, \delta) \right]. \quad (12)$$

The soft wall renormalizes into an error function of width δ , while the variance of the Gaussian potential is increased by δ^2 . Thus, the bigger the width of the potential, the deeper it gets due to the fluctuations, as it allows more flexibility (entropy) in bond formation. For large values of the width δ (highly fluctuating surfaces), the location of the transition point is shifted to $C_1^*/C_2^* = f_c = \sigma_2/\sigma_1 \approx 0.38$. Due to the factor of b^2 in Eq. (12) the net potential gets stronger under RG, and the linear approximation eventually breaks down.

The RG transformation should be extended to a rescaling factor b at which the curvature at the minimum of the renormalized potential is such that the resulting fluctuations in width are comparatively small. Beyond this scale, a quadratic expansion around the minimum of the effective potential should be valid. As demonstrated previously, typical parameters for the synapse yield a bare potential at which the above criterion is (barely) satisfied. Thus the

linear RG approximation is of limited practical value in this context. It may, however, yield interesting information about the global form of the phase diagram as the concentrations C_1^* and C_2^* are further reduced. From the double well shape of the potential, we anticipate that the overall phase diagram consists of a line of discontinuous transitions separating preferences in the synapse for TM or LI bonds. This line is located at $C_1^*/C_2^* \leq 1$ for large concentrations, and moves to $C_1^*/C_2^* \approx \sigma_1/\sigma_2$ at lower concentrations. It presumably terminates at an Ising critical point when the fluctuations in width become of the order of the separation $z_{TM} - z_{LI}$ between the two minima. Sufficiently small values of C_1^* and C_2^* should also result in an unbinding transition which is located at $C_1^*\sigma_1 + C_2^*\sigma_2 \propto \sqrt{k_B T/\gamma}$. It is thus useful to make a more detailed study of the phase diagram of the model synapse as well as the dynamic trajectories as various phase boundaries are approached.

-
- [1] A. K. Abbas, A. H. Lictman, and J. S. Prober, *Cellular and Molecular Immunology* (W.B. Saunders, Philadelphia, 2000).
 - [2] C. R. F. Monks, B. A. Frieberg, H. Kupfer, N. Sciaky, and A. Kupfer, *Nature* **395**, 82 (1998).
 - [3] A. Grakoui, S. K. Bromley, C. Saumen, M. M. Davis, A. S. Shaw, P. M. Allen, and M. L. Dustin, *Science* **285**, 221 (1999).
 - [4] M. F. Krummel, M. D. Sjaastad, C. Wulfing, and M. M. Davis, *Science* **289**, 1349 (2000).
 - [5] K. H. Lee, A. D. Holdorf, M. L. Dustin, A. C. Chan, P. M. Allen, and A. S. Shaw, *Science* **295**, 1539 (2002).
 - [6] S. Stoll, J. Delon, T. M. Brotz, and R. N. Germain, *Immunity* **15**, 691 (2001).
 - [7] E. Hailman, W. R. Burack, A. S. Shaw, M. L. Dustin, and P. M. Allen, *Immunity* **16**, 1 (2002).
 - [8] L. I. Ritchie, P. J. R. Ebert, L. C. Wu, M. F. Krummel, J. T. Owen, and M. M. Davis, *Immunity* **16**, 595 (2002).
 - [9] S. Qi, J. T. Groves, and A. K. Chakraborty, *Proc. Natl. Acad. Sci. (USA)* **98**, 6548 (2001).
 - [10] C. Wulfing and M. M. Davis, *Science* **283**, 2266 (1998).
 - [11] M. L. Dustin and A. S. Shaw, *Science* **283**, 649 (1999).
 - [12] Y. Hori, S. Raychaudhuri, and A. K. Chakraborty, *J. Chem. Phys.* **117**, 9491 (2002).
 - [13] D. N. Garboczi, P. Ghosh, U. Utz, Q. R. Fan, W. E. Biddison, and D. C. Wiley, *Nature* **384**, 134 (1996).
 - [14] R. Simson, E. Wallraff, J. Faix, J. Niewohner, G. Gerisch, and E. Sackmann, *Bipphys. J.* **74**, 514 (1998).
 - [15] A. K. Chakraborty, *Science STKE* **2002**, PE10 (2002).
 - [16] T. R. Weikl, J. T. Groves, and R. Lipowsky, *Europhys. Lett.* **59**, 916 (2002).
 - [17] H.-Y. Chen, *cond-mat/0210398* (2002).
 - [18] D. S. Fisher and D. A. Huse, *Phys. Rev. B* **32**, 247 (1985).
 - [19] R. Lipowsky and M. E. Fisher, *Phys. Rev. Lett.* **10**, 2411 (1986).
 - [20] R. Lipowsky and M. E. Fisher, *Phys. Rev. B* **36**, 2126 (1987).